



Fractal-based brain tumor detection in multimodal MRI

Khan M. Iftekharuddin^{a,*}, Jing Zheng^a, Mohammad A. Islam^a, Robert J. Ogg^b

^a *Intelligent Systems and Image Processing (ISIP) Laboratory, Electrical and Computer Engineering Department, University of Memphis, Memphis, TN 38152, USA*

^b *Department of Diagnostic Imaging, St. Jude Children's Research Hospital, Memphis, TN 38105, USA*

Abstract

In this work, we investigate the effectiveness of fusing two novel texture features along with intensity in multimodal magnetic resonance (MR) images for pediatric brain tumor segmentation and classification. One of the two texture features involves our Piecewise-Triangular-Prism-Surface-Area (PTPSA) algorithm for fractal feature extraction. The other texture feature exploits our novel fractional Brownian motion (fBm) framework that combines both fractal and wavelet analyses for fractalwavelet feature extraction. We exploit three MR image modalities such as T1 (gadolinium-enhanced), T2 and FLuid-Attenuated Inversion-Recovery (FLAIR), respectively. The extracted features from these multimodality MR images are fused using Self-Organizing Map (SOM). For a total of 204 T1 contrast-enhanced, T2 and FLAIR MR images obtained from nine different pediatric patients, our successful tumor segmentation is 100%. Our experimental results suggest that the fusion of fractal, fractalwavelet and intensity features in multimodality MR images offers better tumor segmentation results when compared to that of just fractal and intensity features in single modality MR images. Next, we exploit a multi-layer feedforward neural network with automated Bayesian regularization to classify the tumor regions from non-tumor regions. The Receiver Operating Characteristic (ROC) curves are obtained to evaluate tumor classification performance. The ROC suggests that at a threshold value of 0.7, the True Positive Fraction (TPF) values range from 75% to 100% for different patients, with the average value of 90%.

© 2008 Elsevier Inc. All rights reserved.

Keywords: Image segmentation; Fractal analysis; Multi-resolution texture; Feature fusion; Magnetic resonance imaging; Multi-resolution wavelets; Tumor classification; Receiver Operating Characteristic curve; Neural network

1. Introduction

Brain tissue and tumor segmentation in MR images has been an active research area [1–3]. In general, the problem of image segmentation involves clustering of similar feature vectors [4,5]. Extraction of good features is thus fundamental to successful image segmentation. The segmentation task becomes more challenging when one wants to derive common decision boundaries on different object types in a set of images. Due to the complex structures of different tissues such as white matter (WM), gray matter (GM) and cerebrospinal fluid

* Corresponding author.

E-mail address: iftexhar@memphis.edu (Khan M. Iftekharuddin).

(CSF) in the brain MR images, extraction of useful features is a demanding task. Intensity is an important feature in discriminating different tissue types in the brain MR images. However, using intensity feature alone to segment complex brain tissues and tumor in a single modality MR image has been proved to be insufficient [2,3,6–8]. One of the advantages of MR image over other medical images is that it is easier to obtain multimodality MR images via measuring different independent parameters such as longitudinal relaxation time, transverse relaxation time or proton density. Depending on different parameters measured, the image contains different contrast and spectral appearance. Thus, the multimodality MR images provide more information than single modality image. Consequently, multi-spectral MR image [9,10] offers improved image segmentation results compared to that in single modality image.

In a study of segmenting cortex gray matter in the brain, the deformable surface algorithms offer better results [11,12] when compared to the intensity-based algorithms. Zadeh and Windham [5] have developed an automatic method for the adaptive enhancement and unsupervised segmentation of different brain tissues such as CSF, GM and WM in synthetic MR images. Algorri and Flores-Mangas [13] have also used fuzzy parameters to segment normal brain tissue. While there are considerable amount of works in the literature that provide good segmentation results for normal brain tissues [4,5,13–16], the segmentation of the pathological regions such as tumor and edema in MR images remains a challenging task due to uncertainties associated with tumor location, shape, size and texture properties. Fletcher-Heath et al. [17] have used Fuzzy c-means (FCM) clustering technique, followed by knowledge-guided image processing steps to segment the tumor regions in MR images. In Ref. [17], the authors successfully segment tumor regions in 35 out of a total of 36 slices containing tumor and the volume match between the segmented regions and ground truth regions ranges from 53% to 90%. However, the technique in Ref. [17] may not be useful to detect small tumors since it requires the tumor regions to appear in at least three consecutive slices. Liu et al. [18] have developed an image segmentation and tumor volume measurement method based on the fuzzy-connectedness theory that requires a prior knowledge of the estimated location of the tumor. Mazzara et al. [19] have used a supervised k-nearest neighbor (KNN) method and an automatic knowledge-guided (KG) method to segment the brain tumor in MR images. Compared to the segmentation results generated by physician, the average segmentation accuracy is 56% and 52% for KNN and KG methods, respectively. Prastawa et al. [20] have developed an automatic segmentation method that use atlas as geometric prior to segment the tumor as well as edema. In Ref. [20], the overlap between the segmented tumor region and manually labeled ground truth ranges from 70% to 80%.

The texture features have been explored to characterize and segment the dystrophic muscles and adipose tissue [21–23]. Lerski et al. [24] have demonstrated a brain tumor MR image analysis technique, while Mahmoud-Ghoneim et al. [25] have proposed a 3D co-occurrence matrix based tumor texture analysis with increased specificity and sensitivity. However, in both of their works, the volume of interests needs to be segmented manually. Pachai et al. [26] have proposed a multi-resolution pyramid algorithm to segment multiple sclerosis lesions in the brain MR image with good morphological accuracy and improved reproducibility compared to the manual segmentation method. Pitiot et al. [27] have presented a texture based MR image segmentation approach with a novel combination of a two-stage hybrid neural classifier. The authors show that their correct classification result varies from 90% to 98% for caudate nucleus, hippocampus and corpus callosum. However, the sensitivity and specificity of the system are not discussed.

Among many other texture analysis methods, fractal dimension (FD) analysis is a useful tool in characterizing textural images and surface roughness [28]. In Ref. [29], the authors exploit FD in quantifying the cortical complexity of the brain in clinical groups. We have also successfully exploited the fractal models in analyzing brain tumor in MR images [1,30,31]. It has been reported that the dynamics of tumor growth follows a fractal process [32]. Further, the stochastic fractal Brownian motion (fBm) [33], which offers a framework for integration of fractal and multi-resolution analysis, can successfully describe the tumor characteristics, etc. [34]. Thus, the fractal analysis combining with multi-resolution analysis (MRA) is a promising candidate in characterizing the content of an image in general and segmenting the tumor in particular [1,30,34–36].

In this work, we show that the fusion of our novel fractal features along with intensity values in multimodal MR images provides better brain tumor segmentation and classification. We exploit the effectiveness of our two novel fractal and fractalwavelet features to segment and classify tumor regions from non-tumor regions

in both single and multimodality pediatric brain MR images. The fractal feature is obtained using our previously proposed Piecewise-Triangular-Prism-Surface-Area (PTPSA) algorithm [30,31]. The fractalwavelet feature, on the other hand, is computed using our novel fBm model that integrates both fractal and multi-resolution wavelet analysis for tumor tissue detection [34,35]. We first normalize the image intensity values to correct the possible bias in 2D cross-sections of MR images [37,38]. Then, three types of features such as intensity, fractal and fractalwavelet are extracted from the normalized images. The features are fused and the segmented tumor clusters are obtained exploiting a Self-Organizing Maps (SOM) neural network. After the segmentation, the clusters are labeled as tumor or non-tumor segments. These labeled segments are divided into training and test sets to build a multi-layer feedforward classifier for each of the successfully segmented patient datasets. Receiver Operating Characteristic (ROC) curve is obtained next to evaluate the performance of each classifier.

This paper is organized as follows: in Section 2, we introduce the related background and in Section 3, we discuss the methods and implementation details of the system. The results are presented in Section 4. Section 5 provides the discussion of results. The conclusion and future works are presented in Section 6.

2. Background review

We first discuss the intensity normalization techniques for MR image, and then review the basic concept of fractal and fractalwavelet features to extract texture information from MR images. We also discuss our relevant novel algorithms for extracting fractal and fractalwavelet features. Next, we discuss the Self-Organizing Map (SOM) algorithm that clusters these texture and intensity features to segment brain MR images. We further present a brief description for a feedforward backpropagation classifier to classify segmented images into tumor/non-tumor tissue.

2.1. Intensity standardization

One drawback for MR imaging is that there lacks a standard interpretation for the intensity value in MR image, even within the same protocol for the same body region obtained on the same scanner for the same patient [37,38]. Therefore, in our work, an intensity normalization technique that standardizes the intensity value in MR image is necessary for the subsequent feature extraction and tumor segmentation. Nyul et al. [37] have proposed a two-step intensity standardization technique which transforms the images in a way that the similar intensity values in the transformed image will have similar tissue meaning. A more recent study of MR image intensity standardization technique can be found in Ref. [38]. Another drawback of MR imaging is the intensity inhomogeneity such that the intensity values measured from homogeneous tissue region are not always uniform. Since the intensity inhomogeneity problem mostly affects the intensity-based image analysis techniques, we do not consider the intensity inhomogeneity correction in our work. In our work, we have followed the approach in Refs. [37,38] for MR intensity normalization with satisfactory results.

2.2. Fractal feature

The concept of fractal is first proposed by Mandelbrot [39] to describe the complex geometry of the objects in nature. Fractal dimension (FD) is a real number that describes the fractal property of the object. Unlike the dimensions in Euclidian geometry, FD is not restricted to be an integer; instead, an object's FD is usually a real number whose value depends on the property of the object. Different FD values indicate different texture structures in the image. Usually, the more complex the texture structure is, the higher its FD value will be [30]. The FD has been successfully exploited in different medical image analysis areas such as the evaluation of the cortical complexity [29] and the detection of small lung tumor [40]. There are several different methods to calculate the FD, such as box-counting, modified box-counting, piecewise modified box-counting and piecewise triangular prism surface area (PTPSA) [31]. We have successfully investigated the PTPSA method [30,31] to discriminate the tumor regions from non-tumor regions by their different FD values [31,35] in the single modality image segmentation. In this work, we exploit the PTPSA algorithm to calculate FD on the multimodality image and compare these results with that of using single modality image.

In PTPSA algorithm, an image is first divided into several equal-sized rectangular sub-images with each sub-image has a side length of r . For each of these sub-images, the intensity values of four corner pixels such as p_1 , p_2 , p_3 and p_4 are measured. Then the magnitudes of these intensity values are considered as the heights in the third dimension for each corresponding corner pixel. The average intensity value of these four corner pixels pc is considered as the height in the third dimension for the center pixel of this sub-image. Thus, we can form four triangular such as ABE, BCE, CDE and DAE as shown in Fig. 1 and the FD is calculated as

$$FD = \frac{\log(S_{ADE} + S_{ABE} + S_{BCE} + S_{CDE})}{\log r}, \tag{1}$$

where S represents the surface area of each triangles and the subscript letters represent the apexes of the triangles.

2.3. Fractalwavelet feature

Fractalwavelet feature is based on the fractional Brownian motion (fBm) model, which is a technique that combines both fractal and multi-resolution image decomposition. We have successfully investigated a novel fBm model to extract multi-resolution fractal features from brain MRI [1,34–36]. The fBm is a part of the set of $1/f$ processes, which are the generalization of the ordinary Brownian motion $B_H(S)$. The fBm is non-stationary, zero-mean Gaussian random functions, which are defined as

$$B_H(0) = 0, \tag{2}$$

$$B_H(t) - B_H(s) = \frac{1}{\Gamma(H + 0.5)} \left\{ \int_{-\infty}^0 [(t-s)^{H-0.5} - s^{H-0.5}] dB(s) + \int_0^{\infty} (t-s)^{H-0.5} dB(s) \right\}, \tag{3}$$

where $0 < H < 1$ is the Hurst coefficient that characterizes the fBm. t and s represent different observation times of the process B_H , Γ is the Gamma function.

When the associated correlation function, rB_H , is not exclusively a function of the difference observation times, the fBm is a non-stationary process and can be defined as

$$rB_H(t, s) = E[B_H(t)B_H(s)] = \frac{V_H}{2} (|t|^{2H} + |s|^{2H} - |t-s|^{2H}); \quad 0 < H < 1, \tag{4}$$

where $E[\bullet]$ is the expected value operator, and,

$$V_H = \Gamma(1 - 2H) \frac{\cos(\pi H)}{\pi H}. \tag{5}$$

The non-stationary property suggests that an fBm may not be associated to a spectrum using a standard spectral density computation for estimating the signal power contents. Although fBm is a non-stationary process,

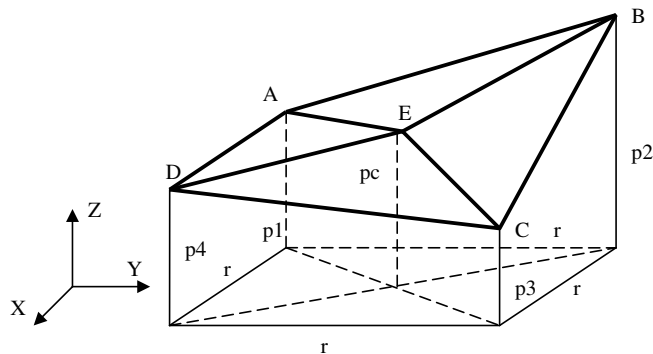


Fig. 1. Piecewise-Triangular-Prism-Surface-Area (PTPSA) algorithm.

its increments are stationary. The stationary property can be observed in fBm's variance function, which is defined as

$$E\left[|B_H(t) - B_H(s)|^2\right] = V_H(t-s)^{2H}, \quad (6)$$

where V_H is defined in Eq. (6). The fBm increments are also self-similar, which means that the following equation can be satisfied at any scale value of α :

$$B_H(t + \alpha\tau) - B_H(t) = \alpha^H B_H(\tau). \quad (7)$$

The previous properties of fBm can be extended to multiple dimensions case. For the two-dimensional case, let $B(\vec{u})$ represent an fBm, where \vec{u} represents the position (u_x, u_y) of a point in a two-dimensional process satisfying the following conditions:

(a) The process is non-stationary if its correlation is not a function of $|\vec{u} - \vec{v}|$ as follows:

$$rB_H(\vec{u}, \vec{v}) = E[B_H(\vec{u})B_H(\vec{v})] = \frac{V_H}{2} (|\vec{u}|^{2H} + |\vec{v}|^{2H} - |\vec{u} - \vec{v}|^{2H}). \quad (8)$$

(b) The increments of the process $\Delta B(\vec{u}) = B(\vec{u} + \Delta\vec{u}) - B(\vec{u})$ forms a stationary, zero-mean Gaussian process and

(c) The variance of the increments $\Delta B(\vec{u})$ depends only on the distance $\Delta u = \sqrt{\Delta u_x^2 + \Delta u_y^2}$, such that

$$E[|\Delta B_H(\vec{u})|^2] \propto \Delta u_H. \quad (9)$$

The stationary and self-similarity of fBm suggest that the time-frequency signal decomposition techniques such as multi-resolution analysis (MRA) is a good candidate for fractal signal analysis. Therefore, the fBm analysis can be performed by estimating H and FD, as follows:

$$FD = D_E + 1 - H, \quad (10)$$

where D_E is the Euclidean dimension that contains the fBm. Eq. (10) suggests that the successful FD computation involves estimation of H . We discuss our novel computational modeling for estimating H , and hence FD, in Section 3.

2.4. The Self-Organizing Maps (SOM) algorithm

In this work, we use Self-Organizing Map (SOM) neural network [41] as the segmentation tool. The SOM learns to cluster input vectors according to how they are naturally grouped in the input space. In its simplest form, the map consists of a regular grid unit which learns to represent the statistical data described by model vectors $x \in \mathfrak{R}^n$, where \mathfrak{R}^n represents n dimension real space. Each map unit i contains a vector m_i ($m_i \in \mathfrak{R}^n$) that is used to represent the data. During the training process the model vectors are changed gradually and finally the map forms an ordered non-linear regression of the model vectors into the data space. At the t th step of the learning process, a data sample $x(t)$ is presented to the grid. Then the node c is searched for the best representation of the sample. The unit c and its neighboring units are updated according to the following learning rule:

$$m_i(t+1) = m_i(t) + h_{ci}(t)[x(t) - m_i(t)], \quad (11)$$

where h_{ci} (usually a symmetric, monotonically decreasing function of the distance of units i and c on the map grid) is the neighboring function expressing how much the unit i is updated when unit c is the winner. This update process continues for all the data samples. As a result of these repeated updates, the model vectors of neighboring map units gradually become similar and eventually the whole grid becomes a globally ordered model vectors. In addition to other advantages of SOM over other clustering approach, the *global ordering* property of SOM is attractive. We observe that when we segment a sequence of brain MR images using SOM, any specific tissue (e.g. GM, WM) or tumor is always grouped into a specific location in the grid. This helps us to label the tumor correctly and unambiguously.

2.5. Neural network classifier

Neural network has been widely used for classification of different tissue regions in medical images [42–44]. In this work, we use multi-layer back propagation neural network as the classifier to discriminate the tumor regions from non-tumor regions. The simplest form of backpropagation algorithm which learns the network's weights and biases is updated in the negative direction of the gradient. The objective function of a standard feedforward neural network is as

$$mse = \frac{1}{N} \sum_{i=1}^N (e_i)^2 = \frac{1}{N} \sum_{i=1}^N (t_i - a_i)^2, \quad (12)$$

where N is the number of sample, t_i is the target output, and a_i is the network output. Similar to any other classifier, the standard backpropagation neural network also suffers from over fitting. This over fitting occurs when the network memorizes the training examples but does not learn to generalize the inputs. To improve the generalization, we obtain the smallest network weights that is large enough to classify the input data with adequate accuracy [45]. We can achieve this by modifying the objective function as follows:

$$msireg = \gamma \times mse + (1 - \gamma) \times msw, \quad (13)$$

where γ is the performance ratio, and

$$msw = \frac{1}{n} \sum_{j=1}^n w_j^2. \quad (14)$$

The objective function in Eq. (13) helps us to build a small network that does not have enough power to over fit. However, how well this function performs depends on the choice of the regularization parameters. In this work, we exploit Bayesian framework [46] to determine the optimal regularization parameters automatically. The weights and biases of the network are assumed to be random variables with specified distributions. Then the unknown variances associated with these distributions are used to estimate the regularization parameters.

2.6. The classifier performance curve

The Receiver Operating Characteristics (ROC) curve is used to quantitatively evaluate the performance of the classifiers [47,48]. From the classifier outputs, we obtain two parameters such as the True Positive Fraction (TPF) and the False Positive Fraction (FPF), at different threshold values for each classifier. TPF is the proportion of the segments that are correctly classified as tumor segment by the classifier while FPF is the proportion of the segments that are incorrectly classified as tumor segment by the classifier. TPF is also known as *sensitivity* while FPF quantitatively equals to $1 - \textit{specificity}$. An ideal classifier with TPF of 1 and FPF of 0 means that this classifier can correctly discriminate all the tumor segments from non-tumor segment while never misclassify the non-tumor segment as the tumor segment. For each classifier, by using the FPF values under different thresholds as the X -coordinates and the corresponding TPF values as the Y -coordinates, a series of points can be obtained, each of which corresponds to one TPF – FPF pair under a certain threshold. The ROC curve is then obtained by connecting all these points. The ROC curve represents the tradeoff between TPF and FPF and describes how well the classifier can discriminate the tumor regions from non-tumor regions. For a good classifier, the corresponding ROC curve should be close to upper-left corner of the plane wherein $TPF \rightarrow 1$ and $FPF \rightarrow 0$.

3. Methods

The goal in this study is to investigate the effectiveness of fusing our novel fractal-based features along with intensity features for improved tumor segmentation and classification in multimodal pediatric brain MR images. In order to satisfy this goal, we propose the following four steps such as: (i) MR image intensity normalization, (ii) feature extraction, (iii) multimodal feature fusion and image segmentation, and (iv) tumor classification. The corresponding overall algorithm flow diagram is shown in Fig. 2. The implementation details of the modules are briefly discussed in the following subsections.

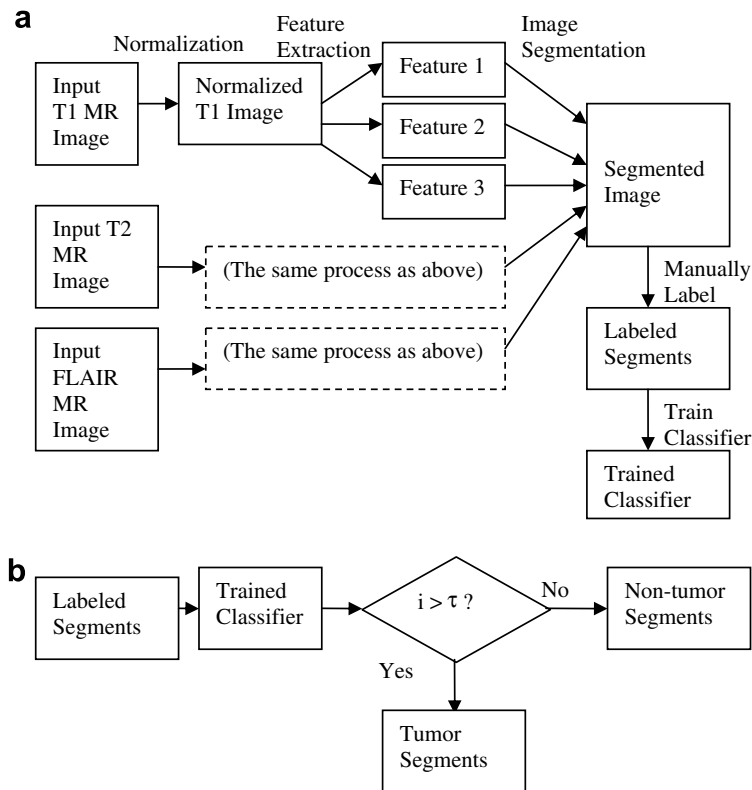


Fig. 2. Flow diagram of the automated tumor identification algorithm (a) the training process and (b) the testing process. The labeled segments in testing process are obtained via the same procedures as that are shown in the training process.

3.1. Image intensity standardization

To alleviate the intensity bias in MR image, an intensity normalization algorithm is necessary as the pre-processing step. In this project, as mentioned in Section 2.1, we implement a two-step normalization method [38], wherein the image histograms are modified such that the histograms match a mean histogram obtained using the training data. After applying this normalization method, the intensity values for the same tissue in different MR images fall into a very narrow range (ideally, a single value) in the normalized images.

3.2. Feature extraction

After intensity standardization, we extract three features from the normalized MR images such as intensity, fractal dimension and fractalwavelet. We compute these features on each 2D cross-section of MR images for all nine patients in our image database. The FD feature is computed using our previously proposed Piecewise-Triangular-Prism-Surface-Area (PTPSA) algorithm [30,31] while the fractalwavelet feature is obtained using our novel fBm-based algorithm [34,35] as discussed in Section 2.

3.2.1. PTPSA algorithm

The flow diagram for PTPSA algorithm is shown in Fig. 3. In Fig. 3, we first divide each 2D MR image slice into 8×8 sub-image. The remaining steps follow the derivation in Section 2.2. Note that for PTPSA algorithm, the choice of size of sub-image affects the FD calculation result [31]. Based on our extensive statistical experimentation on the effect of sub-image size in computing FD using fractal algorithm, we choose 8×8 as the sub-image size that offers the most significant difference in FD values between tumor and non-tumor regions [31].

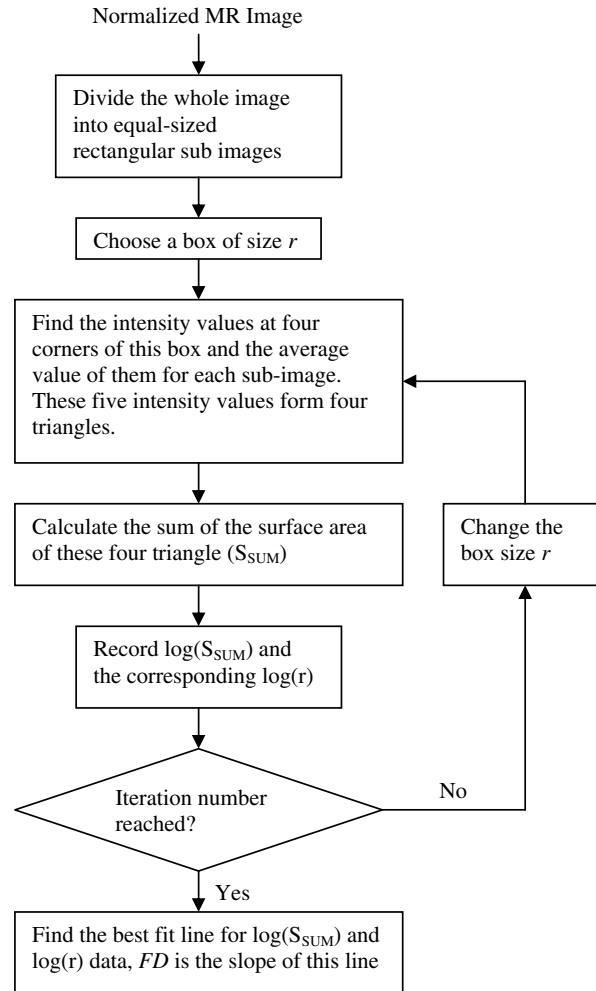


Fig. 3. The flow diagram for PTPSA algorithm.

3.2.2. The fBm variance model and algorithm

In this section, we discuss our novel fBm-variance model [34,35] to estimate H , and hence FD , as we have mentioned in Section 2.3. We estimate the fractal features through the computation of the variance of detail coefficients in a multi-resolution decomposition scheme [34]. For an approximation resolution at scale 2^j , the multi-resolution representation of an fBm process in Eq. (3) is given by

$$B_H(t) = 2^{j/2} \sum_n a_j[n] \phi(2^{-j}t - n) + \sum_j 2^{-j/2} \sum_n n d_j[n] \psi(2^{-j}t - n), \quad (15)$$

where $j = -J, \dots, \infty$, $n = -\infty, \dots, +\infty$. $\phi(t)$ is the scaling function, $a_j[n]$ and $d_j[n]$ are the j th scale approximate and detail coefficients, respectively. The two-dimensional extension of the detail coefficients, at the j th scale resolution, can be written as [1]

$$D_{2^j}^3[n, m] = 2^{-j} \int_{-\infty}^{+\infty} \int_{-\infty}^{+\infty} B_H(x, y) \psi_{2^j}^3(x - 2^{-j}n, y - 2^{-j}m) dx dy, \quad (16)$$

where $\psi_{2^j}^3$ corresponds to the two-dimensional wavelet associated to the diagonal detail filter. Rewriting Eq. (16) yields

$$D_{2^j}^3[\vec{n}] = 2^{-j} \int_{-\infty}^{+\infty} B_H(\vec{u}) \psi_{2^j}^3(\vec{u} - 2^{-j}\vec{n}) d\vec{u}, \quad (17)$$

where η corresponds to the position $[n, m]$ and $\psi_{2^j}^3$ satisfies the admissibility condition [49],

$$\int_{-\infty}^{+\infty} \int_{-\infty}^{+\infty} \psi_{2^j}^3(x, y) dx dy = 0. \tag{18}$$

The variances function of the detail coefficients in Eq. (16) is obtained following a similar process to the continuous wavelet approach as follows:

$$E[|D_{2^j}^3[\vec{\eta}]|^2] = 2^{-2j} \int_u \int_v \psi_{2^j}^3(\vec{u} - 2^{-j}\vec{\eta}) \psi_{2^j}^3(\vec{v} - 2^{-j}\vec{\eta}) E[B(\vec{u})B(\vec{v})] d\vec{u} d\vec{v}. \tag{19}$$

The variance of the two-dimensional detail signal $D_{2^j}^3[\vec{\eta}]$ can be considered as a power law of the scale 2^j and can be used to calculate the Hurst coefficient, H , in a similar way. Thus, we obtain

$$\log_2 E[|D_{2^j}^3[n, m]|^2] = (2H + 2)j + C_2, \tag{20}$$

where

$$C_2 = \log_2 \frac{V_H}{2} V_{\psi_{2^j}^3}(H). \tag{21}$$

The H value of the two-dimensional fBm process can be extracted from the slope of the variance as a function of the order of the resolution scale— j . Finally, FD is obtained using Eq. (10). The corresponding algorithm implementation is shown in Fig. 4. In order to compute the FD using our fBm variance algorithm in Fig. 4, we

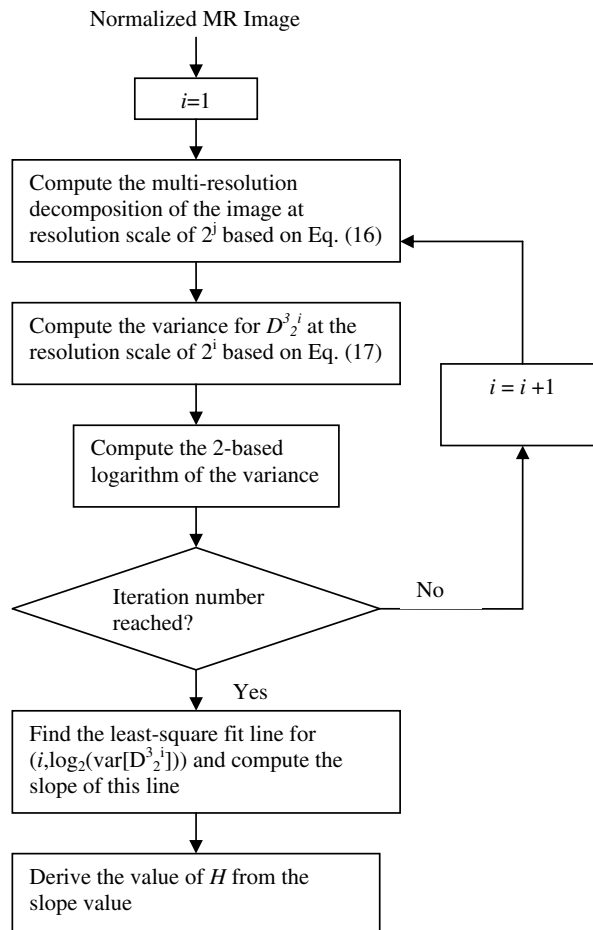


Fig. 4. The flow diagram for calculating FD of two-dimension fBm process.

consider three levels of scale decomposition in the MRA. We also consider 8×8 sub-image size at the full resolution of 2D image slice for our fractalwavelet-based FD computation.

3.3. Multimodal feature fusion and tumor segmentation

We exploit *Self-Organizing Map (SOM)* as our feature fusion and segmentation tool. A single feature, such as intensity, is not sufficient to discriminate one tissue type from the others in a SOM setup. Further, the intermediate experimental results (not shown here) show that the selection of a threshold in SOM algorithm that increases the *TPF* also increases the *FPF* at the same time if only one single feature is used. To alleviate this rather intricate problem, we use the combination of two (intensity and fractal) or three (intensity, fractal and fractalwavelet) features as the input features to the SOM algorithm. The output of the SOM algorithm offers the segmented clusters. In SOM algorithm, we only need to provide approximate number of clusters since the algorithm itself can automatically choose the optimal number of clusters as well as the optimal shape of the grid. This flexibility is useful since it is difficult to know the optimal number of clusters without running the segmentation algorithm repeatedly. After the segmentation, each segment is labeled as tumor or non-tumor segments and these labeled segments are then used for classifier training and testing.

3.4. The tumor classification

We investigate a feedforward neural network with automated Bayesian regularization as the classifier to discriminate the tumor from the non-tumor regions. For each segment, the mean values of the three features (intensity, fractal dimension and fractalwavelet) are calculated and these feature values are used as the input vectors to the classifier. The output of the classifier suggests presence/absence of tumor in a MR image sequence. Specifically, a classifier output that is close to ‘one’ suggests a tumor segment while the output that is close to ‘zero’ suggests non-tumor segment. In our experiment, we observe that the variance values of all three features for all the clusters are negligible. Thus, mean values alone sufficiently represent these clusters. To evaluate the classifier performance, the half of the labeled segments is used as the training set while the other half is used as the testing set. We build a total of nine classifiers, each of which corresponds to the tumor data from nine different patients, respectively. Finally, ROC curves are investigated to ascertain the classifier performance in our study.

4. Results

We first describe our MR brain image database and then show the tumor segmentation results with fractal-based features using multiple and single modality MR image. Finally, we describe the tumor classification results using the segmented images. We also obtain comprehensive classifier performance evaluation using ROC curves.

4.1. Image database

In this work, our image database includes three image modalities such as gadolinium-enhanced T1, T2 and FLAIR, respectively. We analyze a total of 204 brain MR tumor images from nine different pediatric patients, with 68 images for each modality. Summary information of the MR images in our database is shown in Table 1. All of these images are sampled by 1.5 T Siemens Magnetom scanners from Siemens Medical Systems. The slice gap varies from 4 mm to 5 mm, the field-of-view (FOV) is $210 \times 210 \text{ mm}^2$ and the size of each of the image matrix is 256×256 pixels, respectively. The scan parameters for T1-weighted image are: TR = 165 ms, TE = 6 ms, flip angle = 60° ; the scan parameters for T2-weighted image are: Turbo Spin Echo, TR = 6630, TE = 115 ms, 15 echoes per TR.

4.2. Feature extraction results

To evaluate the effectiveness of our novel fractal-based features in discriminating tumor from non-tumor regions, we compute intensity, fractal dimension and fractalwavelet features on each 2D MR tumor image.

Table 1
MR image data statistics

P	Tumor type	Slice thickness (mm)	Number of tumor(s)	Number of image with visible tumors	T1			T2		FLAIR	
					Total number of images	Tumor visibility	Contrast agent	Total number of images	Tumor visibility	Total number of images	Tumor visibility
1	Astrocytoma	4	Single	9	31	Medium	Applied	31	Good	31	Medium
2	GBM	5	Multiple	9	29	Good	Applied	27	Good	27	Good
3	GBM		Single	6	27	Medium	Applied	27	Medium	27	Medium
4	BSG		Single	9	27	Medium	Applied	27	Medium	27	Medium
5	Metastatic tumor		Single	6	31	Good	Applied	25	Good	25	Good
6	JPA		Single	8	27	Medium	Applied	27	Good	27	Medium
7	Craniopharyngioma		Single	8	25	Good	Applied	25	Good	25	Good
8	PXA		Single	6	27	Good	Applied	25	Good	25	Good
9	Cystic-suprasellar mass		Single	7	24	Medium	Applied	25	Medium	25	Medium
T				68	248			239		239	

We obtain feature plots to observe whether these features help to improve the delineation of the tumor region from the non-tumor regions. To plot the feature plot, we first divide the image into equal-sized 8×8 sub-images. For each of these sub-images, we calculate the fractal dimension and fractalwavelet features as described above. We then obtain the normalized mean value of the fractal, fractalwavelet and intensity features for the tumor and non-tumor regions for each of the 2D image slices for a particular patient. Thus, in the feature plot for a specific patient, each data point corresponds to one 2D image slice and the coordinate values of the data point represent the normalized mean feature values for this image. The data points that correspond to the tumor region are labeled black while those correspond to the non-tumor regions are labeled white. Our extensive experimentation with database in Table 1 show that in many 2D MR image slices, while intensity feature alone is useful, adding fractal and/or fractalwavelet to intensity can help to delineate the tumor region better. For example, Figs. 5 and 6 show T1 images wherein intensity feature alone may be used to separate tumor from non-tumor tissues. However, addition of fractal and fractalwavelet features may provide added benefit to delineate tumor regions from that of non-tumor as shown in Figs. 6 and 7, respectively. On the other hand, due to increased contrast in T2 images, intensity alone appears sufficient to separate tumor tissues from the non-tumor tissues as shown in Figs. 8–10, respectively. Further, inclusion of fractal and fractalwavelet features along with intensity helps in better tumor separation from the non-tumor regions and subsequent tumor segmentation as discussed in the following section. Thus, our analysis with all the single modality MR images in Table 1 shows that while intensity feature may be useful in many cases, by adding

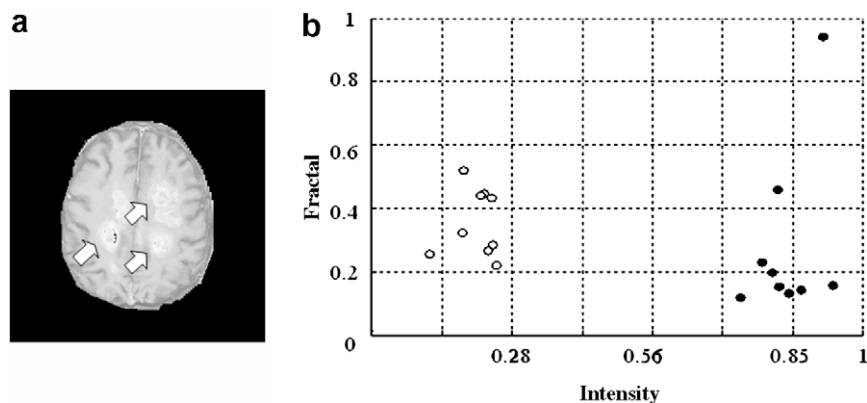


Fig. 5. (a) One example 2D slice of original T1 image for patient #2 and (b) the fractal vs. intensity normalized mean feature plot for all nine slices for patient #2 (white points correspond to the non-tumor region, black points correspond to the tumor region).

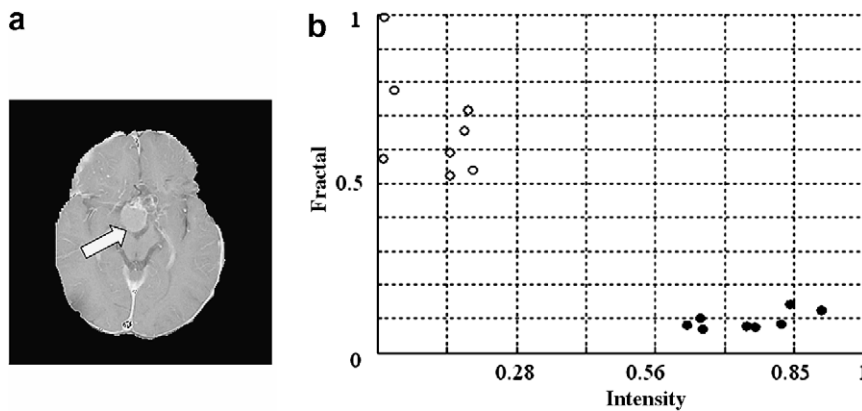


Fig. 6. (a) One example 2D slice of original T1 image for patient #7 and (b) the fractal vs. intensity normalized mean feature plot for all eight slices for patient #7 (white points correspond to the non-tumor region, black points correspond to the tumor region).

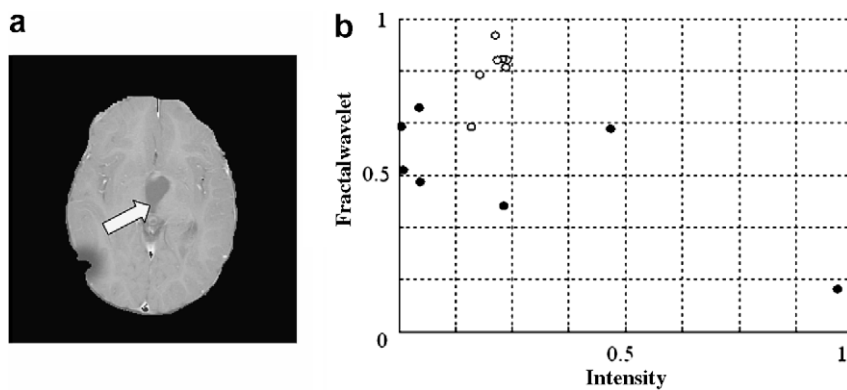


Fig. 7. (a) One example 2D slice of original T1 image for patient #6 and (b) the fractalwavelet vs. intensity normalized mean feature plot for all eight slices for patient #6 (white points correspond to the non-tumor region, black points correspond to the tumor region).

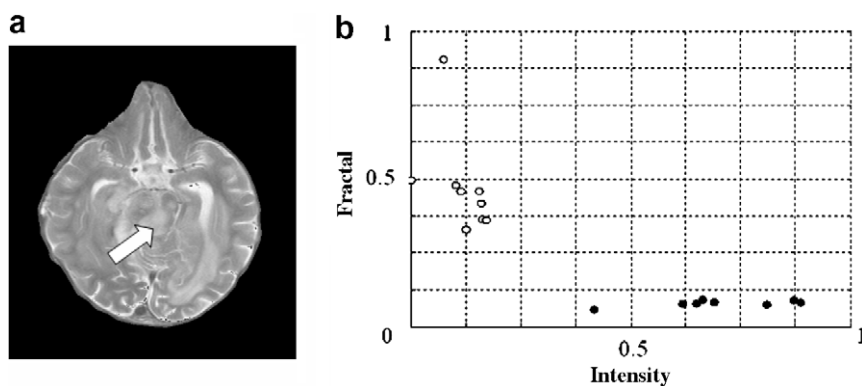


Fig. 8. (a) One example 2D slice of original T2 image for patient #4 and (b) the fractal vs. intensity normalized mean feature plot for all nine slices for patient #6 (white points correspond to the non-tumor region, black points correspond to the tumor region).

fractal and/or fractalwavelet as the additional features, one can improve delineation and subsequent segmentation of tumor regions from those of non-tumor regions. Note that we have extensively studied the statistical significance of fractal features in delineating tumor tissue from that of the non-tumor in [31].

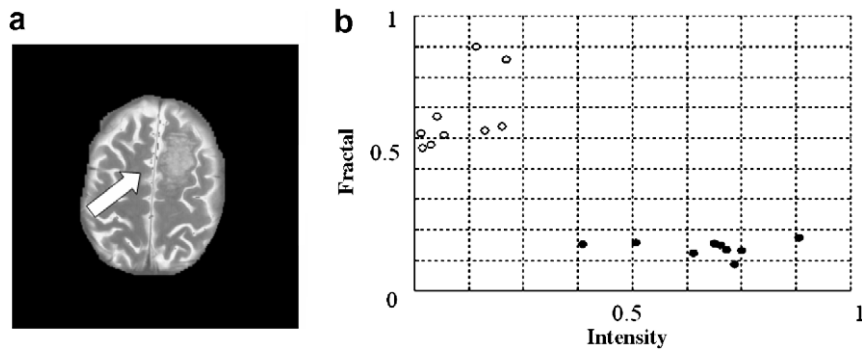


Fig. 9. (a) One example 2D slice of original T2 image for patient #2 and (b) the fractal vs. intensity normalized mean feature plot for all nine slices for patient #2 (white points correspond to the non-tumor region, black points correspond to the tumor region).

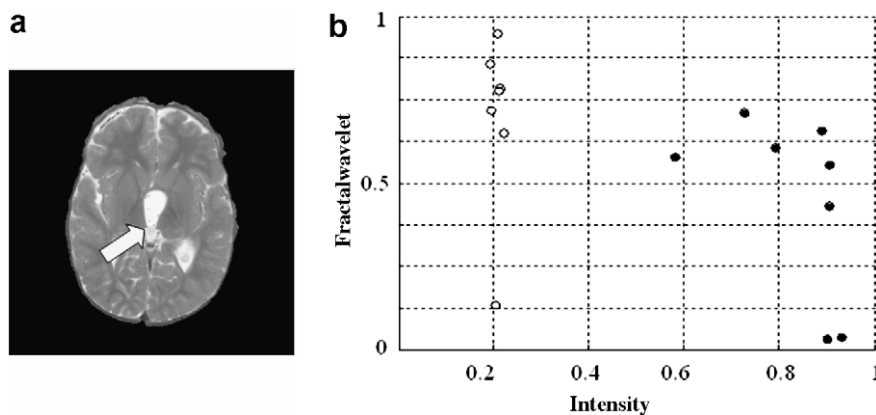


Fig. 10. (a) One example 2D slice of original T2 image for patient #6 and (b) the fractalwavelet vs. intensity normalized mean feature plot for all eight slices for patient #6 (white points correspond to the non-tumor region, black points correspond to the tumor region).

4.3. Multimodality MR feature fusion and tumor segmentation results

We exploit a SOM algorithm to fuse our extracted features and segment the tumor regions. We compare the tumor segmentation results of using different combinations of the features in single modality as well as multimodality MR images. First, we experiment with different feature combinations such as (i) intensity; (ii) intensity and fractal dimension; and (iii) intensity, fractal dimension and fractalwavelet as the input to the SOM for single modality MR image segmentation. The tumor segmentation results for an example T1 image slice is shown in Fig. 11, while that for an example T2 image slice is shown in Fig. 12, respectively. In Fig. 11, the segmentation using intensity alone is not always robust, while the segmentation using fusion of two (intensity and fractal dimension) or three features (intensity, fractal dimension and fractalwavelet) offers better results. Note that either two or three feature fusion results for the example T1 image in Fig. 11 show similar tumor segmentation performance. However, fusion of three features for the example T2 image in Fig. 12 offers better tumor segmentation than that of two features. Comparing the segmentation results in T1 and T2 image, we observe that in T2 images, the tumor segments usually capture more tumor area than those in the T1 images. A summary of the complete segmentation results using single modality T1 and T2 images as well as a combination of multimodality (T1, T2 and FLAIR) MR images are shown in Table 2. For single modality images, the successful tumor segmentation rate ranges from 57% to 95%, depending on different features and image modality combinations. Further, Table 2 suggests that the combination of three features improves the successful tumor segmentation rate when compared to that of two features. Consequently, we only consider the three-feature (intensity, fractal dimension and fractalwavelet) fusion

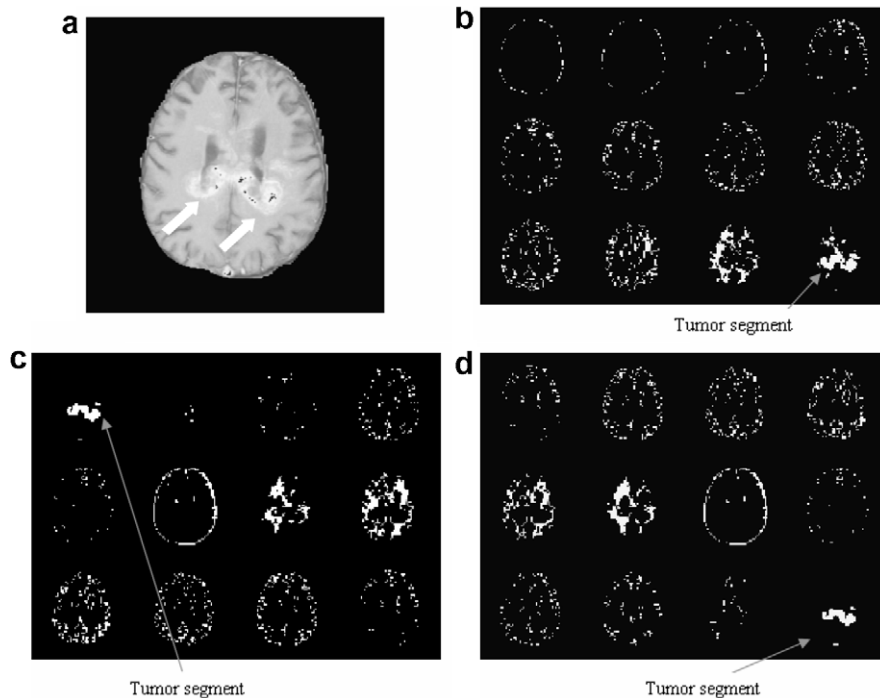


Fig. 11. Tumor segmentation with feature fusion: (a) A 2D T1 image slice from patient #2. Tumor segmentation results using (b) intensity alone; the entire tumor region cannot be clearly segmented. (c) Intensity and fractal features, all the tumor region are clearly segmented and (d) intensity, fractal and fractalwavelet, the entire tumor region is clearly segmented.

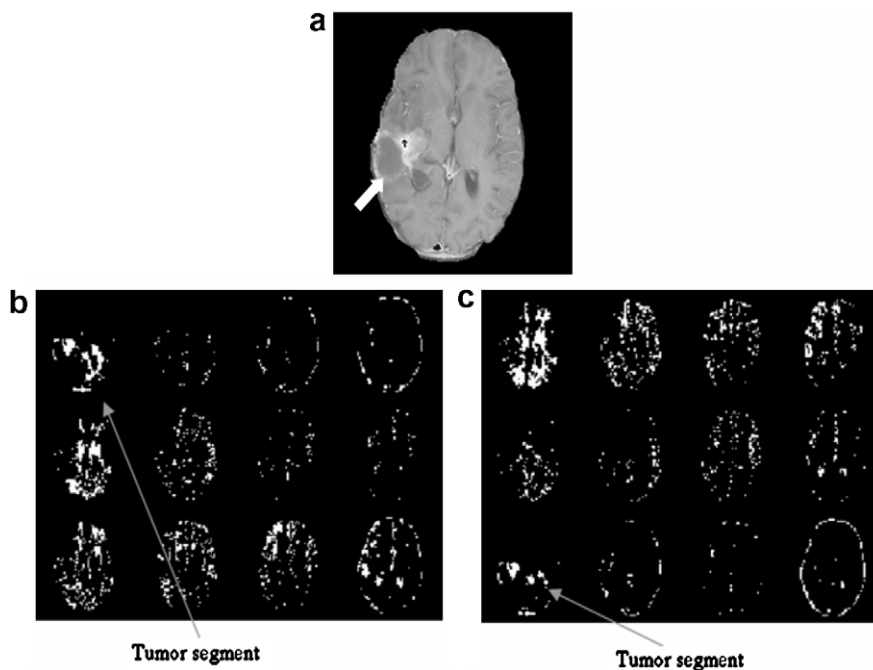


Fig. 12. Tumor segmentation with feature fusion: (a) A 2D T2 image slice from patient #3. Tumor segmentation results using (b) intensity and fractal features; the entire tumor region cannot be clearly segmented; and (c) intensity, fractal and fractalwavelet; the entire tumor region is clearly segmented.

Table 2
Summary of tumor segmentation results

Patient	Single modality				Multimodality
	T1		T2		T1 + T2 + FLAIR
	Intensity + fractal	Intensity + fractal + fractalwavelet	Intensity + fractal	Intensity + fractal + fractalwavelet	Intensity + fractal + fractalwavelet
1	33% (3/9)	44% (4/9)	100% (9/9)	100% (9/9)	100% (9/9)
2	55% (5/9)	55% (5/9)	78% (7/9)	89% (8/9)	100% (9/9)
3	33% (2/6)	67% (4/6)	100% (6/6)	100% (6/6)	100% (6/6)
4	33% (3/9)	33% (3/9)	67% (6/9)	77% (7/9)	100% (9/9)
5	83% (5/6)	100% (6/6)	100% (6/6)	100% (6/6)	100% (6/6)
6	63% (5/8)	75% (6/8)	100% (8/8)	100% (8/8)	100% (8/8)
7	75% (6/8)	75% (6/8)	100% (8/8)	100% (8/8)	100% (8/8)
8	100% (6/6)	100% (6/6)	67% (4/6)	100% (6/6)	100% (6/6)
9	57% (4/7)	57% (4/7)	85% (6/7)	100% (7/7)	100% (7/7)
Total	57% (39/68)	64% (44/68)	88% (60/68)	95% (65/68)	100% (68/68)

The numbers in parenthesis represent the number of images that the tumor region can be clearly segmented vs. the total number of image with visible tumor.

case for multimodality images. The tumor segmentation results using multimodality images with three-feature fusion is shown in the last column of Table 2. Overall, using multimodality image with three-feature fusion significantly improves the tumor segmentation results. For multimodality images, the successful tumor segmentation rates are 100% for all nine patients.

4.4. Tumor classification results

To evaluate the tumor classification performance of our feedforward classifier, we divide the segmented tumor data into two equal halves for training and testing, as mentioned before. We compare the tumor classification results for single modality with that for multimodality MR images, respectively. A summary of ROC curves at three different threshold values for both single modality and multimodality MR images are shown in Table 3. Note that in single modality cases, we do not build classifiers for three patients wherein our SOM segmentation does not provide at least five correct tumor segments for all the images with visible tumor for a particular patient as shown in Table 2. For multimodality image, we construct a total of nine classifiers, each of which corresponds to one patient. Further, for multimodality case, we only consider the case wherein all three features are fused. Table 3 shows that the multimodal MR fusion offers the *TPF* ranging from 75% to 100% with the average value of 90% at the threshold value of 0.7. These results suggest that fusing features in multimodality images improves the tumor detection rate when compared to that of using single modality images.

5. Discussion

The goal in this study is to investigate the effectiveness of fusing our novel fractal-based features [30,34] along with intensity feature for improved tumor segmentation and classification in multimodality pediatric brain MR images. One of the two fractal-based techniques involves our PTPSA algorithm for FD feature

Table 3

Single modality and multimodality images: True Positive Fraction (TPF) and False Positive Fraction (FPF) values at different thresholds for the classifiers

P	Threshold	Single modality								Multimodality					
		T1				T2				T1 + T2 + FLAIR					
		Intensity + fractal		Intensity + fractal + fractalwavelet		Intensity + fractal		Intensity + fractal + fractalwavelet		Intensity + fractal + fractalwavelet					
		TPF	FPF	TPF	FPF	TPF	FPF	TPF	FPF	TPF	FPF				
1	0.5	No classifier is built due to lack of segmented images								1	0	0.67	0	0.8	0.02
	0.7									1	0	0.67	0	0.8	0.02
	0.9									1	0	0.67	0	0.8	0.02
2	0.5	1	0	0.67	0	0.4	0	0.33	0.09	1	0.15				
	0.7	0.5	0	0.67	0	0.4	0	0.33	0.09	1	0.13				
	0.9	0.5	0	0.67	0	0.4	0	0	0.09	1	0.13				
3	0.5	No classifier is built due to lack of segmented images								1	0	1	0.03	0.8	0.07
	0.7									1	0	1	0.03	0.8	0.07
	0.9									1	0	0.67	0.03	0.8	0.05
4	0.5	No classifier is built due to lack of segmented images								0.5	0	0.67	0.22	0.75	0.06
	0.7									0.5	0	0.67	0.13	0.75	0.06
	0.9									0	0	0.67	0	0.75	0.03
5	0.5	0	0.09	0.67	0.42	0.67	0.09	0.67	0.06	1	0				
	0.7	0	0.09	0.67	0.42	0.67	0.09	0.67	0.06	1	0				
	0.9	0	0.09	0.67	0.42	0.67	0.09	0.67	0.06	1	0				
6	0.5	1	0.14	0	0.11	0	0	0	0.02	0.75	0.18				
	0.7	1	0.14	0	0.11	0	0	0	0.02	0.75	0.18				
	0.9	1	0.14	0	0.11	0	0	0	0.02	0.5	0.18				
7	0.5	1	0.15	0.33	0.07	1	0	1	0	1	0.22				
	0.7	0.67	0.15	0.33	0.07	1	0	1	0	1	0.22				
	0.9	0.67	0.15	0.33	0.07	1	0	1	0	1	0.22				
8	0.5	0.67	0	0.33	0	1	0.03	0.67	0	1	0.03				
	0.7	0.67	0	0.33	0	1	0.03	0.67	0	1	0.03				
	0.9	0.67	0	0.33	0	1	0.03	0.67	0	1	0				
9	0.5	0	0	0.5	0.17	1	0.03	0.5	0	1	0				
	0.7	0	0	0.5	0.17	1	0.03	0.5	0	1	0				
	0.9	0	0	0.5	0.17	1	0.03	0.5	0	1	0				

extraction. The other method exploits our novel fBm framework that combines both fractal and wavelet analyses for fractalwavelet feature extraction. For fractalwavelet modeling, we consider Daubechies' basis wavelet with three levels of decomposition. The choice of wavelet bases and the level of decomposition depends on our extensive experimentation that offers better tumor discrimination in FD values [35]. Further, for both fractal and fractalwavelet features in full scale 2D image slices, we choose the sub-image size of 8×8 . The choice of sub-image size in this study is based on our extensive statistical analyses performed on the effect of sub-image size in fractal-based FD values [31].

Intensity is an important feature for automatic tumor detection. However, our study as well as previous works [3,6,8,50] show that in many brain MR image analysis examples, intensity alone is not sufficient to offer satisfactory segmentation results. We analyze a total of 204 multimodal MR images from nine different patients for tumor segmentation. These MR images consist of three modalities such as gadolinium-enhanced T1, T2 and FLAIR, with each of the modality containing visible tumor in 68 image slices. We first experiment with different fusion combinations of three features such as intensity, fractal dimension and fractalwavelet in a SOM network to segment the tumor regions. We observe that when segmented with single modality image, the T2 images offer higher percentage of successful tumor segmentation rate than the T1 images. However, the cluster purity (how much non-tumor region is clustered with the tumor segment) in T1 is better than that in T2. The reason is that the tumor appears bright in most of the T2 images in our image database and, therefore, is easily segmented with the tissues that also appear bright such as CSF. We also find that any single feature may not be sufficient to obtain a clear decision boundary between tumor and non-tumor tissues. Thus,

SOM-based fusion of texture features such as fractal and fractalwavelet along with intensity significantly improves tumor segmentation results for single modality MR images studied in this work. By exploiting fused features in multimodality MR image, 100% tumor segmentation is achieved for all nine patients in our database. Note that for multimodality image fusion, image registration may be an issue in general. However, in this study, each of the classifiers is generated using the multimodality image data from a single patient at a time. Further, the fractal- and fractalwavelet features are both region-based image characteristics, which make the segmentation less sensitive to spatial differences across the modalities. Thus, image registration is not necessary for our current feature fusion approach using SOM.

We investigate automated tumor classification using a feedforward classifier. We label the segmented tumor images and divide the labeled segments into training and test datasets. These two datasets are used as input vectors to train and test a feed-forward neural network classifier, respectively. We also exploit techniques for improving generalization of the feedforward classifier. In brain MR images, the pixel intensity and fractal values of different tissues do not strictly fall into a narrow range. Thus, memorizing the range for the previous training samples is misleading for classifying the future inputs. Consequently, improving generalization is important in the tumor classification applications. Comparing tumor classification performance, multimodality MR images offer better classification results over single modality MR images. We perform extensive classifier performance evaluation using ROC curves. We validate our automated tumor classification results by dividing the tumor segment data into equal halves for training and testing, respectively. Overall, when using multimodality image with fused features, at a threshold of 0.7, the *TPF* for all the nine patients investigated ranges from 75% to 100%, with average value of about 90%, while the *FPF* remains small (<8%) for all nine patients, with the average value of about 1%. This 90% average true tumor classification rate using our fractal-based techniques is either comparable or better than relevant works reported in the literatures [17,20,27,51].

6. Conclusion and future work

In this work, we exploit the effectiveness of fusing two novel fractal-based features with intensity values to segment and classify tumor regions from non-tumor regions in both single modality and multimodality pediatric brain MR images. Our single modality-based technique is useful for the patients wherein multimodality MR image data may not be available. For multimodality MR images, our simulation results show the feature fusion of two novel fractal-based features along with intensity values offer excellent tumor segmentation and classification results when compared to intensity-based segmentation method in single modality MR image.

In the past decade, the fidelity and resolution of medical imaging have experienced dramatic increase [52]. The large number of medical images in modern medical examinations and the relative shortage of the radiologists demand effective tools for computer aided brain image segmentation. The brain tumor segmentation and classification technique developed in this study can be used to scan and ‘flag’ potential tumor in 2D slices from huge number of MR images in a typical brain tumor study. Once the classifiers are trained using our fractal-based technique, these classifiers can then be used to filter out non-suspecting brain scans as well as to point out suspicious regions that have similar property as the tumor regions. The radiologists then may spend time on selected brain scans that are ‘flagged’ by our system. Most of the human interactions time required for this technique such as image intensity standardization, image segmentation, manual labeling of the segments and the classifier training can all be done off-line. The approximate time needed to build a trained classifier for a single patient is about 30 min on a Pentium4 computer with 256 MB of memory. Once the classifier is trained, the subsequent tumor classification task is fully automated.

In order to claim a clinically robust classifier, we need to further improve our algorithm to make it less patient-dependent. This will require us to exploit more effective feature extraction, clustering and classification algorithms. In this research, we consider only clearly visible tumor in our pediatric brain MR image dataset. We need to work with hard-to-detect tumor cases in our dataset. Further, a careful observation on the segmented tumor results reveals that our existing feature vectors may not be sufficient to discriminate multiple types of brain tissues such as white matter, gray matter, CSF and skull from solid tumor and edema. Thus, we plan to exploit additional discriminating features for tumor and multi-tissue classification.

Acknowledgements

This work was supported in part by the Whitaker Foundation through Biomedical Engineering Research Grants RG-01-0125 and TG-04-026. The authors would like to express appreciation to St. Jude Children's Research Hospital for providing the pediatric brain MR images for this work.

References

- [1] K.M. Iftakharuddin, On techniques in fractal analysis and their applications in brain MRI, in: T.L. Cornelius (Ed.), *Medical imaging systems: technology and applications, Analysis and Computational Methods*, vol. 1, World Scientific Publications, 2005, ISBN 981-256-993-6.
- [2] L.P. Clarke, R.P. Velthuizen, M.A. Camacho, J.J. Heine, M. Vaidyanathan, L.O. Hall, R.W. Thatcher, M.L. Silbiger, MRI segmentation: methods and applications, *Magn. Reson. Imaging* 13 (3) (1995) 343–368.
- [3] J.C. Bezdek, L.O. Hall, L.P. Clarke, Review of MR image segmentation techniques using pattern recognition, *Med. Phys.* 20 (4) (1993) 1033–1048.
- [4] H.S. Zadeh, H.S. Windham, Optimal linear transformation for MRI feature extraction, *IEEE Trans. Med. Imaging* 15 (1996) 749–767.
- [5] H.S. Zadeh, J.P. Windham, A comparative analysis of several transformations for enhancement and segmentation of magnetic resonance image scene sequences, *IEEE Trans. Med. Imaging* 11 (N3) (1992) 302–318.
- [6] D. Wang, D.M. Doddrell, A segmentation-based partial-volume-compensated method for an accurate measurement of lateral ventricular volumes on T1-weighted magnetic resonance images, *Magn. Reson. Imaging* 19 (2001) 267–272.
- [7] X. Zeng, L.H. Staib, R.T. Schultz, J.S. Duncan, Segmentation and measurement of the cortex from 3-D MR images using coupled-surfaces propagation, *IEEE Trans. Med. Imaging* 18 (10) (1999) 927–937.
- [8] M. Just, M. Thelen, Tissue characterization with T1, T2 and proton density values: results in 160 patients with brain tumors, *Radiology* 169 (1988) 779–785.
- [9] M.W. Vannier, R.L. Butterfield, D. Jordan, W.A. Murphy, R.G. Levitt, M. Gado, Multispectral analysis of magnetic resonance images, *Radiology* 154 (1) (1985) 221–224.
- [10] M.W. Vannier, T.K. Pilgram, C.M. Speidel, L.R. Neumann, D.L. Rickman, L.D. Schertz, Validation of magnetic resonance imaging (MRI) multispectral tissue classification, *Comput. Med. Imaging Graph.* 15 (4) (1991) 217–223.
- [11] D. MacDonald, N. Kabani, D. Avis, A.C. Evans, Automated 3-D extraction of inner and outer surfaces of cerebral cortex from MRI, *Neuroimage* 12 (3) (2000) 340–356.
- [12] B. Fischl, M.I. Sereno, R.B. Tootell, A.M. Dale, High-resolution intersubject averaging and a coordinate system for the cortical surface, *Hum. Brain Mapp.* 8 (4) (1999) 272–284.
- [13] M.E. Algorri, F. Flores-Mangas, Classification of anatomical structures in MR brain images using fuzzy parameters, *IEEE Trans. Biomed. Eng.* 51 (9) (2004) 1599–1608.
- [14] D.L. Pham, J.L. Prince, Adaptive fuzzy segmentation of magnetic resonance images, *IEEE Trans. Med. Imaging* 18 (9) (1999) 737–752.
- [15] Y. Zhang, M. Brady, S. Smith, Segmentation of brain MR images through a hidden Markov random field model and the expectation-maximization algorithm, *IEEE Trans. Med. Imaging* 20 (1) (2001) 45–57.
- [16] K. Van Leemput, F. Maes, D. Vandermeulen, P. Suetens, Automated model-based tissue classification of MR images of the brain, *IEEE Trans. Med. Imaging* 18 (10) (1999) 897–908.
- [17] L.M. Fletcher-Heath, L.O. Hall, D.B. Goldgof, F.R. Murtagh, Automatic segmentation of non-enhancing brain tumors in magnetic resonance images, *Artif. Intell. Med.* 21 (1–3) (2001) 43–63.
- [18] J. Liu, J.K. Udupa, D. Odhner, D. Hackney, G. Moonis, A system for brain tumor volume estimation via MR imaging and fuzzy connectedness, *Comput. Med. Imaging Graph.* 29 (1) (2005) 21–34.
- [19] G.P. Mazzara, R.P. Velthuizen, J.L. Pearlman, H.M. Greenberg, H. Wagner, Brain tumor target volume determination for radiation treatment planning through automated MRI segmentation, *Int. J. Radiat. Oncol. Biol. Phys.* 59 (1) (2004) 300–312.
- [20] M. Prastawa, E. Bullitt, S. Ho, G. Gerig, A brain tumor segmentation framework based on outlier detection, *Med. Image Anal.* 8 (3) (2004) 275–283.
- [21] S. Herlidou, Y. Rolland, J.-Y. Bansard, E.L. Rumeur, J.-D.d. Certains, Comparison of automated and visual texture analysis in MRI: characterization of normal and diseased skeletal muscle, *Magn. Reson. Imaging* 17 (9) (1999) 1393–1397.
- [22] D. Mahmoud-Ghoneim, J.-D.d. Certains, S. Herlidou, Y. Rolland, A. Maniere, A gender difference on magnetic resonance imaging texture analysis of human adipose tissue, *J. Wom. Imag.* 3 (2001) 105–107.
- [23] P.A. Eliat, D. Mahmoud-Ghoneim, J.-D.d. Certains, Texture analysis and metabolic magnetic resonance imaging, *Trends Appl. Spect.* 4 (2002) 1–20.
- [24] R.A. Lerski, K. Straughan, L.R. Schad, D. Boyce, S. Bluml, I. Zuna, MR image texture analysis: an approach to tissue characterization, *Magn. Reson. Imaging* 11 (1993) 873–887.
- [25] D. Mahmoud-Ghoneim, G. Toussint, J. Constans, J.-D.d. Certains, Three dimensional texture analysis in MRI: a preliminary evaluation in gliomas, *Magn. Reson. Imaging* 21 (2003) 983–987.

- [26] C. Pachai, Y.M. Zhu, J. Grimaud, M. Hermier, A. Dromigny-Badin, A. Boudraa, G. Gimenez, C. Confavreux, J.C. Froment, A pyramidal approach for automatic segmentation of multiple sclerosis lesions in brain MRI, *Comput. Med. Imaging Graph.* 22 (5) (1998) 399–408.
- [27] A. Pitiot, A. Toga, N. Avache, P. Thompson, Texture based MRI segmentation with a two-stage hybrid neural classifier, in: *Proceedings of the World Congress on Computational Intelligence/INNS-IEEE International Joint Conference on Neural Networks WCCI-IJCNN*, 2002.
- [28] N. Sarkar, B.B. Chaudhuri, An efficient approach to estimate fractal dimension of textural images, *Pattern Recognit.* 23 (1992) 1035–1041.
- [29] P.M. Thompson, A.D. Lee, R.A. Dutton, J.A. Geaga, K.M. Hayashi, M.A. Eckert, U. Bellugi, A.M. Galaburda, J.R. Korenberg, D.L. Mills, A.W. Toga, A.L. Reiss, Abnormal cortical complexity and thickness profiles mapped in Williams syndrome, *J. Neurosci.* 25 (16) (2005) 4146–4158.
- [30] K.M. Iftekharuddin, W. Jia, R. March, Fractal analysis of tumor in brain MR images, *Mach. Vis. Appl.* 13 (2003) 352–362.
- [31] J.M. Zook, K.M. Iftekharuddin, Statistical analysis of fractal-based brain tumor detection algorithms, *J. Magn. Reson. Imaging* 23 (2005) 671–678.
- [32] A. Bru, J.M. Pastor, Super-rough dynamics on tumor growth, *Phys. Rev. Lett.* 81 (18) (1998) 4008–4011.
- [33] B.B. Mandelbrot, J.W.V. Ness, Fractional Brownian motions, fractional noises and applications, *SIAM Rev.* 10 (4) (1968) 422–437.
- [34] K.M. Iftekharuddin, C. Parra, Multiresolution-fractal feature extraction and tumor detection: analytical modeling and implementation, in: *Proceedings of the 47th Annual SPIE Meeting, Optical Science and Technology*, San Diego, CA, 2003.
- [35] K.M. Iftekharuddin, M.A. Islam, J. Shaik, C. Parra, R. Ogg, Automatic brain tumor detection in MRI methodology and statistical validation, in: *Proceedings of the Progress in Biomedical Optics and Imaging, Medical Imaging, Image Processing*, San Diego, CA, 2005.
- [36] C. Parra, K.M. Iftekharuddin, R.Kozma, Automated brain data segmentation and pattern recognition using ANN, in: *Proceedings of the Second International Conference on Computational Intelligence, Robotics and Autonomous Systems (CIRAS)*, Singapore, 2003.
- [37] L.G. Nyul, J.K. Udupa, X. Zhang, New variants of a method of MRI scale standardization, *IEEE Trans. Med. Imaging* 19 (2) (2000) 143–150.
- [38] A. Madabhushi, J.K. Udupa, Interplay between intensity standardization and inhomogeneity correction in MR image processing, *IEEE Trans. Med. Imaging* 24 (5) (2005) 561–576.
- [39] B.B. Mandelbrot, *The Fractal Geometry of Nature*, Freeman, San Francisco, CA, 1983.
- [40] S. Kido, K. Kuriyama, M. Higashiyama, T. Kasugai, C. Kuroda, Fractal analysis of internal and peripheral textures of small peripheral bronchogenic carcinomas in thin-section computed tomography: comparison of bronchioloalveolar cell carcinomas with nonbronchioloalveolar cell carcinomas, *J. Comput. Assist. Tomogr.* 27 (1) (2003) 56–61.
- [41] T. Kohonen, *Self-organization and Associative Memory*, second ed., Springer-Verlag, Berlin, 1987.
- [42] B.K. Szabo, P. Aspelin, M.K. Wiberg, Neural network approach to the segmentation and classification of dynamic magnetic resonance images of the breast: comparison with empiric and quantitative kinetic parameters, *Acad. Radiol.* 11 (12) (2004) 1344–1354.
- [43] H. Sujana, S. Swarnamani, S. Suresh, Application of artificial neural networks for the classification of liver lesions by image texture parameters, *Ultrasound Med. Biol.* 22 (9) (1996) 1177–1181.
- [44] Y. Zhu, H. Yan, Computerized tumor boundary detection using a Hopfield neural network, *IEEE Trans. Med. Imaging* 16 (1) (1997) 55–67.
- [45] H. Demuth, M. Beale, *Neural Networks Toolbox User's Guide*, Mathwork Inc., 1998.
- [46] D.J.C. Mackay, Bayesian interpolation, *Neural Comput.* 4 (3) (1992) 415–447.
- [47] T. Kubota, Y. Ushijima, K. Yamada, C. Okuyama, O. Kizu, T. Nishimura, Diagnosis of Alzheimer's disease using brain perfusion SPECT and MR imaging: which modality achieves better diagnostic accuracy? *Eur. J. Nucl. Mol. Imaging* 32 (4) (2005) 414–421.
- [48] B. Bengtsson, D. Bizios, A. Heijl, Effects of input data on the performance of a neural network in distinguishing normal and glaucomatous visual fields, *Invest. Ophthalmol. Vis. Sci.* 46 (10) (2005) 3730–3736.
- [49] S.G. Mallat, A theory for multiresolution signal decomposition: the wavelet representation, *IEEE Trans. Pattern Anal. Mach. Intell.* 11 (7) (1989) 674–693.
- [50] L.O. Hall, A.M. Bensaïd, L.P. Clarke, R.P. Velthuizen, M.L. Silbiger, J.C. Bezdek, A comparison of neural networks and fuzzy clustering techniques in segmenting magnetic resonance images of the brain, *IEEE Trans. Neural Networks* 3 (1992) 672–683.
- [51] M. Prastawa, E. Bullitt, N. Moon, K. Van Leemput, G. Gerig, Automatic brain tumor segmentation by subject specific modification of atlas priors, *Acad. Radiol.* 10 (12) (2003) 1341–1348.
- [52] C.L. Partain, H.P. Chan, J.G. Gelovani, M.L. Giger, J.A. Izatt, F.A. Jolesz, K. Kandarpa, K.C. Li, M. McNitt-Gray, S. Napel, R.M. Summers, G.S. Gazelle, Biomedical imaging research opportunities workshop II: report and recommendations, *Radiology* 236 (2) (2005) 389–403.